CHEMISTRY
A EUROPEAN JOURNAL

ChemPubSoc
Europe

DOI: 10.1002/chem.201202272

Hemin-Functionalized Reduced Graphene Oxide Nanosheets Reveal Peroxynitrite Reduction and Isomerization Activity

Amit A. Vernekar and Govindasamy Mugesh*[a]

Abstract: Facile and efficient reduction of graphene oxide (GO) and novel applications of the reduced graphene oxide (RGO) based materials are of current interest. Herein, we report a novel and facile method for the reduction of GO by using a biocompatible reducing agent dithiothreitol (DTT). Stabilization of DTT by the formation of a six-membered ring with internal disulfide linkage upon oxidation is responsible for the reduction of GO. The reduced graphene oxide is characterized by several spectroscopic and microscopic techniques. Dispersion of RGO in DMF remained stable for several weeks suggesting that the RGO obtained by DTT-mediated reduction is hydrophobic in nature. This method can be considered for large scale production of good quality RGO. Treatment of RGO with hemin afforded a functional hemin-reduced graphene oxide (H-RGO) hybrid material that exhibited remarkable protective effects against the potentially harmful peroxynitrite (PN). A detailed inhibition study on PN-mediated oxidation and nitration reactions indicate that the interaction between hemin and RGO results in a synergistic effect, which leads to an efficient reduction of PN to nitrate. The RGO also catalyzes the isomerization of PN to nitrate as the RGO layers facilitate the rapid recombination of $^{\bullet}NO_2$ with $Fe^{IV}=O$ species. In the presence of reducing agents such as ascorbic acid, the $Fe^{IV}=O$ species can be reduced to Fe^{III}, thus helping to maintain the PN reductase cycle.

Keywords: antioxidants · graphene · hemin · nanosheets · peroxynitrite

Introduction

Graphene, a single atom thick and 2D material has attracted significant interest in the areas of materials science and biology.[1] The remarkable electronic and mechanical properties, high surface area and high conductivity led to the use of graphene in nanoelectronics, nanocomposites, nanophotonics, energy storage, catalysis, biosensors, and drug delivery.[1] To exploit these attributes, a large scale production of superior quality graphene sheets is highly desirable. Wide variety of approaches to produce graphene have been established in recent literature like chemical vapor deposition (CVD),[2a,b] micromechanical exfoliation of graphite,[2c] epitaxial growth,[2d] and liquid-phase exfoliation.[2e] Chemical reduction of graphene oxide (GO) has marked an impact on the generation of copious quantity of reduced graphene oxide (RGO) with cost effectiveness.[3] $NaBH_4$,[3b,c] N_2H_4,[3d,e] hydroquinone,[3f] dimethyl hydrazine,[1b] and Fe/HCl[3g] have been shown to reduce GO. However, great care is essential while using these highly toxic and explosive reducing agents. Furthermore, formation of adducts with the introduction of other functionalities and metal impurities in RGO have been noticed during the use of these reducing agents, which affect the electrical properties of graphene and their use in biological and biochemical applications.

Functionalization of graphene with polar molecules imparts the hydrophilicity over hydrophobic effects, and thus enhances its dispersibility in polar solvents.[1h] Particularly, noncovalent functionalization of graphene with biomolecules decipher the graphene to be highly biocompatible with the conservation of intrinsic properties of graphene.[1j] Hemin, a well-known protoporphyrin found at the active sites of heme proteins, plays a key role in biochemical reactions and electron-transport chain. Hemin and related metalloporphyrins have been shown to exhibit peroxidase-like and antioxidant activities.[4] Recently, hemin-functionalized graphene nanosheets have been shown to exhibit peroxidase activity, to differentiate ss- and ds-DNA,[5a] to oxidize pyrogallol effectively,[5b] to selectively and quantitatively detect cancer cells.[5c] Herein, we describe a new method for the reduction GO using dithiothreitol (DTT) as reducing agent. DTT is a remarkably strong reducing agent (in comparison to the glutathione, cysteine, and so on) with redox potential of −0.33 V at pH 7. We also demonstrate, for the first time, that hybrid nanosheets obtained by functionalization of RGO with hemin exhibit remarkable peroxynitrite (PN) isomerase and reductase-like antioxidant activities.

[a] A. A. Vernekar, Prof. Dr. G. Mugesh
Department of Inorganic and Physical Chemistry
Indian Institute of Science
Bangalore 560 012 (India)
E-mail: mugesh@ipc.iisc.ernet.in

Supporting information for this article is available on the WWW under http://dx.doi.org/10.1002/chem.201202272.

Results and Discussion

The GO required for the synthesis of RGO was obtained using the Hummers method.[6] Ultrasonication of GO in water resulted in homogeneous dispersion of GO, which was further subjected to the reduction process. DTT as a reducing agent was then added to the aqueous dispersion of GO. Reduction process in the neutral conditions led to only partial reduction of GO. DTT appears to be an active reducing agent in the alkaline pH range due to the formation of reactive thiolate upon deprotonation. Scheme 1 shows the reduction of GO to RGO in the presence of DTT. An enhancement of the reduction rate was observed upon addition of ammonia as a base in this reaction. This result is consistent with the earlier report in which facile deoxygenation of GO has been shown to occur under alkaline conditions.[7] The strong reducing properties of DTT have been attributed to its ability to form intramolecular disulfide bond. Although GO has been shown to oxidize thiols to dilsufides in non-aqueous media, the route yields carbon materials that are not nanosheets.[8] Therefore, water appears to be a preferable medium for the exfoliation of graphite oxide and reduction of GO to get RGO nanosheets.

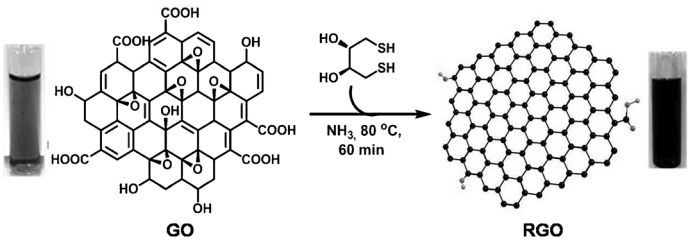

Scheme 1. Schematic representation of the synthesis of RGO by the reduction using DTT.

Color change of the GO dispersion from brown to black in the presence of DTT was the preliminary observation that indicates the formation of RGO (see Scheme 1 and Scheme S1 in the Supporting Information for a color figure). The formation of RGO was confirmed by UV/Vis spectroscopy. Figure 1 A shows the UV/Vis spectra of GO and RGO. The dispersion of GO in water exhibits a maximum absorption at 230 nm, which could be attributed to the π–π^* transition resulting from C=C bonds of aromatic skeleton. A broad shoulder in the 290–300 nm region corresponds to the n–π^* transition of C=O bonds from the carboxylic acid functionalities on GO. Reduction of GO using DTT shifts the maximum absorption from 230 nm to 267 nm due to the restoration of conjugation that was distorted in GO. Furthermore, disappearance of the shoulder accounting for the C=O bond that appeared in GO confirms the deoxygenation process and removal of carboxylic acid groups. An increase in the absorbance was also observed due to the reduction after 60 min at 80 °C. A similar reduction carried out at room temperature (28 °C) resulted in partial reduction of GO and hence, high temperature was employed in the study. The reduction was further confirmed by FT-IR analysis. Figure 1 B shows the comparative IR spectra of GO and RGO. A strong absorption band at 1728 cm^{-1} is exhibited by GO due to the stretching of C=O. A broad band in the region 3600–3200 cm^{-1} corresponding to the O–H stretching vibrations is also observed along with O–H deformation vibration at 1389 cm^{-1}. Stretching vibrations at 1618 cm^{-1} and 1043 cm^{-1} are attributed to the C=C and C–O units in GO, respectively. In contrast, RGO showed no characteristic absorption for vibrations from C=O. A dramatic decrease in the absorption of C–O and O–H groups was observed, indicating the effective reduction of GO to RGO.

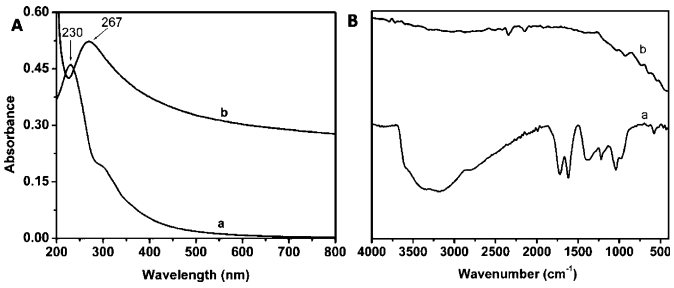

Figure 1. A) UV/Vis absorption spectra and B) FTIR spectra of a) GO and b) RGO.

Raman scattering is an essential technique to characterize the structural electronic properties of graphite and graphene based materials. Chemical oxidation of pristine graphite to GO followed by the reduction of GO to RGO induces enormous structural changes which could be followed by Raman spectra. Figure 2 a shows the Raman spectra of pristine graphite, GO and RGO. The G band due to the first order scattering of the E_{2g} phonons of sp^2 carbon atoms (1575 cm^{-1}) and D band originating from a breathing mode of k-point photons of A_{1g} symmetry are the two main characteristic features of graphene based materials.[3g,9] In this study, the G band for the pristine graphite appeared at 1573 cm^{-1} as the sole characteristic for the first order scattering of the E_{2g} mode. Oxidation of graphite resulted in broadening and shifting of the G band to 1587 cm^{-1} in GO.

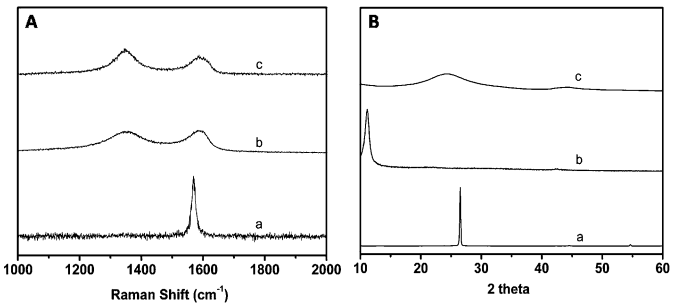

Figure 2. A) Raman spectra and B) XRD patterns of a) graphite, b) GO, and c) RGO.

In addition to the G band, a prominent D band is also observed at 1349 cm^{-1}, which is ascribed to the destruction of sp^2 character and extensive oxidation induced defects in sheets. After the reduction of GO by DTT, the Raman spectra of RGO still exhibits D and G bands at 1347 cm^{-1} and 1583 cm^{-1}, respectively. The ratio of the intensities of D to G band (I_D/I_G) is found to be 0.98 in case of GO. Interestingly, there was a small increase in the I_D/I_G ratio for RGO (1.06) upon reduction of GO. The major effect of deoxygenation, restoration of the sp^2 network and existence of small and isolated aromatic domains are responsible for the observed increase in the I_D/I_G ratio in RGO.[3g,9c,10] It should be noted that this ratio is lower than those reported for the RGO produced using $NaBH_4$ (>1),[3c] N_2H_4 (1.63),[11] hydroquinone (>2),[3f] pre-reduction by $NaBH_4$ (1.91).[12] The I_D/I_G ratio is comparable to those obtained for solvothermal route (1.16),[13] hydrothermal method (0.90),[14] GO/$NaBH_4$/H_2SO_4/annealing (0.82).[12] It has been shown recently that the reduction of GO by Fe/HCl is an effective method resulting in I_D/I_G ratio equal to 0.32 for RGO obtained after 360 min of reduction time.[3g] A comparison between I_D/I_G ratios of RGO obtained via different routes is shown in Table 1.

Table 1. Comparison of I_D/I_G ratios of RGO obtained by different methods.

Reducing agent/methods	I_D/I_G	References
N_2H_4	1.63	[11]
$NaBH_4$	>1	[3c]
Na + EtOH (solvothermal)	1.16	[13]
hydroquinone	>2	[3f]
L-cysteine	1.2	[15]
dextran	1.03	[16]
GO/$NaBH_4$/H_2SO_4 annealing at 1100 °C	0.82	[12]
Fe/HCl	0.32	[3g]
baker's yeast	1.44	[17]
DTT	1.06	this work

To gain some insights into the structure of RGO, the distance between the two layers of RGO was calculated. The X-ray diffraction (XRD) patterns of pristine graphite, GO and RGO are given in Figure 2B. Pristine graphite exhibits only a single peak (002) at $2\theta = 26.5°$ with d spacing = 0.335 nm. Introduction of oxygen functionalities on either sides of RGO sheets upon oxidation of graphite and intercalation of water molecules shifts the 002 reflection peak to lower angle $2\theta = 11.1°$ with d spacing = 0.796 nm. Upon reduction of GO by DTT, the 002 reflection peak of graphite oxide disappears and the broad peak appears at $2\theta = 24.3°$ with d spacing = 0.366 nm corresponding to the exfoliation of the layered RGO sheets. To further understand the thickness of layers, atomic force microscopy (AFM) and transmission electron microscopy (TEM) were employed (see below).

To illustrate the formation of RGO, we further employed X-ray photoelectron spectroscopy (XPS) to study the deoxygenation process. Deconvolution of the C1s spectrum of GO

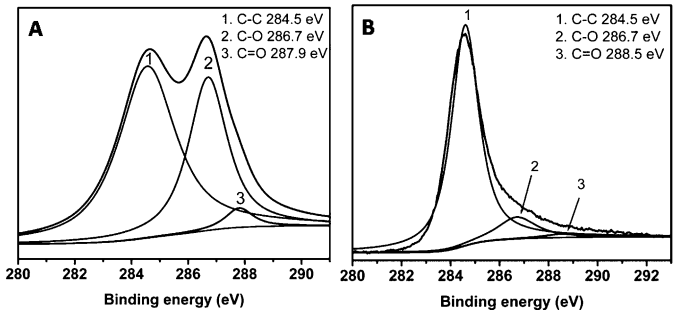

Figure 3. Deconvoluted C1s XPS spectra of A) GO B) RGO.

(Figure 3A) clearly indicates the extensive degree of oxidation. C=C/C−C of aromatic rings, C−O, and C=O groups show signals at 284.5, 286.7, and 287.9 eV, respectively. Upon reduction of GO by DTT, a dramatic decrease in the intensities of all C1s signals of the oxygen bound carbons and sp^3 carbon (Figure 3B) was observed, suggesting the deoxygenation of majority of oxygen containing functional groups. In addition, the increase in intensity of sp^2 carbon peak indicates that the distortion in conjugation induced upon oxidation in GO is restored after reduction by DTT. In this regard, DTT appears to be a much better candidate for the reduction of GO as compared to the monothiol glutathione.[18]

A comparison between the thermal stabilities of GO, RGO and graphite was also studied by thermogravimetric analysis (TGA; Figure 4). The TGA profile obtained for

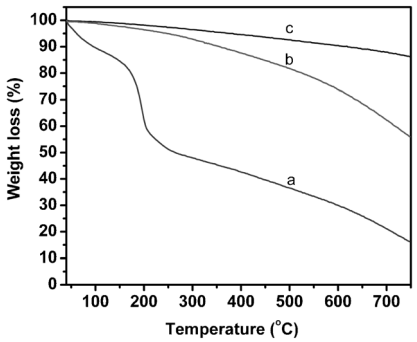

Figure 4. TGA profiles of a) GO, b) RGO, and c) graphite.

GO shows a mass loss of 11% at 100 °C, which can be attributed to the loss of adsorbed and intercalated water molecules between GO layers. A significant increase in the weight loss was observed in the temperature range 170–240 °C due to the removal of thermally labile functional groups like hydroxyl or epoxy, in the form of CO, CO_2, or water vapor.[19] In contrast, RGO exhibited pronounced thermal stability due to the prior deoxygenation of labile functional groups by DTT. A weight loss of 3.5% is shown by RGO in Ar gas flow at 200 °C, which is much less as compared to that shown by GO. This suggests the presence of lower amount of oxygen containing functionalities as a

result of effective reduction. This loss is comparable to pristine graphite showing 2% weight loss at 200°C. Interestingly, the weight loss at 200°C for RGO is less than that reported for the reduction using monothiols such as glutathione (ca. 10%),[18] cysteine (ca. 10%),[15] and other reducing agent such as urea (>10%).[20] This indicates that DTT is a more efficient reducing agent than the monothiol counterparts and urea due to the reactive dithiolates formed in the reaction and assisted stability of the formation of stable six-membered ring after its oxidation. A 25% weight loss at 600°C of RGO may be attributed to the pyrolysis of carbon skeleton, which is similar to that observed for GO and graphite.

The SEM, TEM, and HRTEM images of RGO are shown in Figure 5. The SEM image (Figure 5A) of solid powder of RGO on carbon tape reveals the randomly oriented and

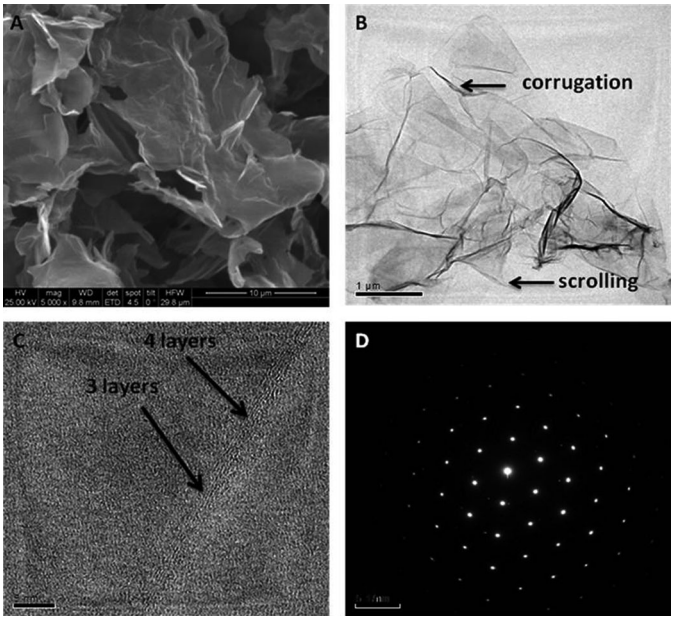

Figure 5. A) SEM, B) TEM, C) HRTEM, D) SAED pattern of RGO nanosheets. TEM image reveals the corrugation and scrolling of nanosheets. Few layers are seen in HRTEM image. The SAED pattern corresponds to image C.

thin curved sheets. Due to the low resolution limit of SEM and the use of solid powder sample, this data do not prove well to view individual sheets of RGO. Therefore, TEM samples were prepared by casting a drop of dispersion of RGO in ethanol on a Cu grid. RGO nanosheets were seen as crumpled silk veil waves as shown in Figure 5B, which is consistent with earlier report.[3f] Bending of graphene sheets is a result of thermodynamic stability of the 2D membrane giving rise to corrugation and scrolling as intrinsic feature of graphene sheets.[21] The thickness of RGO is found to be around 1–2 nm consisting of few (2–4 layers) layers stacked individual graphene sheets due to its inherent scrolling and folding nature as shown in HRTEM image (Figure 5C). Selected area electron diffraction (SAED) pattern of RGO shows a perfect six-fold symmetry as shown in the Figure 5D. The well-defined diffraction pattern further indicates the crystalline nature of the RGO. Intensity differences in the diffraction spots suggest the formation of few layers of RGO due to its intrinsic nature of formation of stacks.[22]

Atomic force microscopy (AFM) has been used routinely to study the surface morphology, thickness of sheets and to identify number of layers of graphene sheets. Figure 6 displays the AFM image recorded after casting a sonicated RGO dispersion drop on freshly cleaved mica surface. The thickness of RGO has been determined to be 0.67 nm corresponding to a single layer of RGO. This thickness is consistent with that reported earlier for single layer graphene.[23]

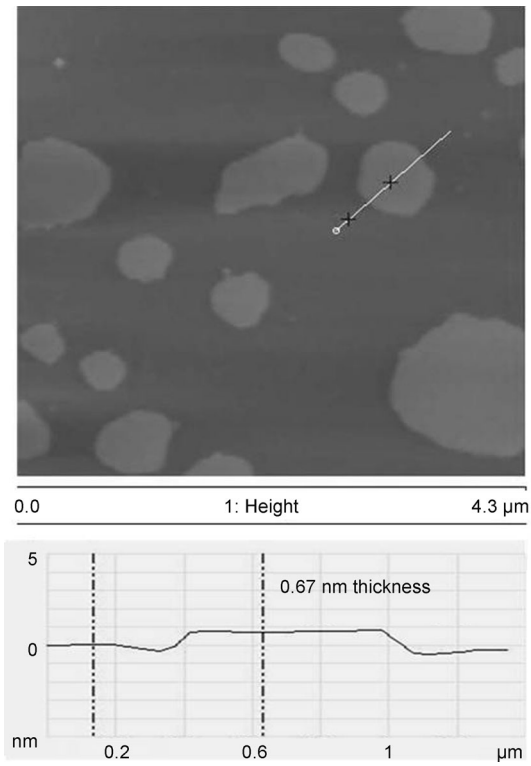

Figure 6. AFM image of RGO with cross section showing 0.67 nm thickness of one of the several sheets.

To further confirm the formation of RGO, we have carried out ^{13}C MAS NMR study. In the ^{13}C NMR spectra of GO (Figure 7), the signals at 59.94 and 68.58 ppm can be attributed to ^{13}C nuclei bearing epoxide and hydroxyl groups, respectively.[23b–e] Graphitic or unoxidized sp^2 carbon exhibited a peak at 130.29 ppm and the carbonyl carbon displayed its resonance at 190 ppm. A small peak at 166.90 ppm may arise from O=C-O groups (ester carbonyl) as shown by Gao et al.[12] Interestingly, all the above signals originating from the oxygenated and carbonyl carbons disappeared after the reduction of GO by DTT. The appearance of broad resonance from 50–150 ppm, thus, confirms the resto-

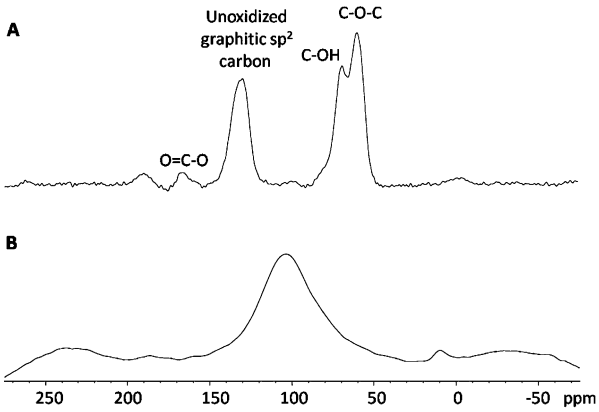

Figure 7. Solid-state ^{13}C MAS NMR spectra of A) GO and B) RGO.

ration of sp^2 carbons and formation of RGO. This result supports the data obtained from XRD, XPS, TG.

Owing to the higher propensity of polar groups on GO, it is highly soluble in water than in organic solvents. Upon reduction of GO with DTT, the RGO sheets formed were well dispersible in DMF than in water confirming the hydrophobic nature of RGO (Figure 8A). This dispersion remained stable for several weeks than in water where faster agglomeration was observed. Furthermore, the RGO dispersion in DMF shows a Tyndall effect on shining a red laser beam (Figure 8A), which confirms the colloidal nature of RGO dispersion. Similar observations were also reported by Gao et al.[12] Further, we also studied the effect of salt on the dispersibility of RGO. Addition of a salt (NaCl) solution to the dispersion of RGO (Figure 8B) resulted in quick agglomeration of RGO suggesting the efficient removal of oxygen containing functionalities from GO by DTT (Figure 8C). This type of salt effect on dispersion of graphene has also been shown previously by Li et al.[24]

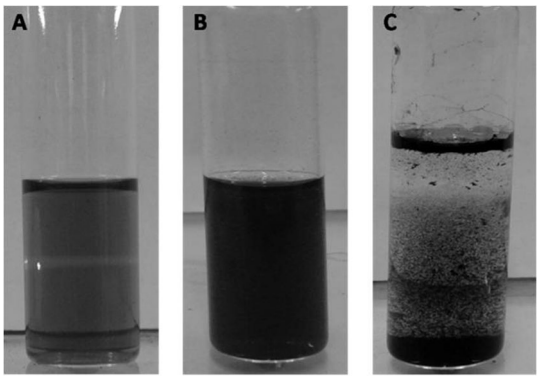

Figure 8. A) Colloidal dispersion of RGO in DMF exhibits Tyndall effect upon shining a laser beam. B) Dispersion of RGO prepared after ultrasonication for 1.5 h in water, which was stable for few minutes. C) Addition of salt (NaCl) solution to the RGO dispersion in water led to the immediate precipitation of RGO.

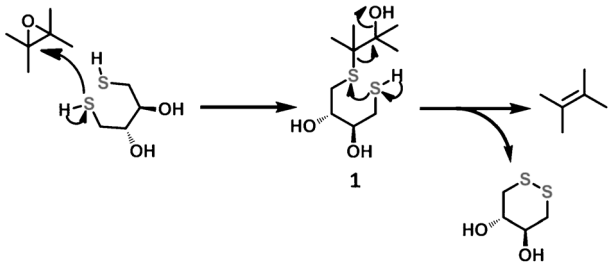

Scheme 2. Proposed mechanism of the reduction of GO by DTT.

The reduction of GO by DTT may follow a mechanism shown in Scheme 2. The deprotonation of DTT under basic condition results in the formation of reactive thiolates, which can behave as potent nucleophiles. In an interaction of DTT thiolates with GO, the epoxy ring is first opened up after an attack of one of the thiolates to give intermediate **1**. Due to the thermodynamic stability of the formation of six-membered ring (DTT_{ox}), the rapid cyclization of DTT results in the reduction of GO. In addition to this, the exothermic nature of the reaction plays a role in achieving further aromaticity by the removal of hydroxyl and carbonyl groups. The formation of oxidized DTT (DTT_{ox}) was confirmed by HPLC (Figure S1–S3 in the Supporting Information).

Although RGO is hydrophobic in nature, it can be readily functionalized to impart hydrophilic behavior and high dispersibility in aqueous media.[1h] Non-covalent functionalization provides a hybrid material having a high dispersibility without adversely affecting the intrinsic properties of graphene.[1j] Particularly, functionalization of graphene sheets with biomolecules not only improves their dispersibility in aqueous media, but also renders them to be biocompatible with novel properties originating from the combined effects of graphene and functionalized molecules. Accordingly, hemin, a redox active moiety found at the active sites of heme proteins was stabilized on RGO sheets by noncovalent functionalization through π--π stacking interactions to yield H-RGO hybrid nanosheets (Scheme 3).

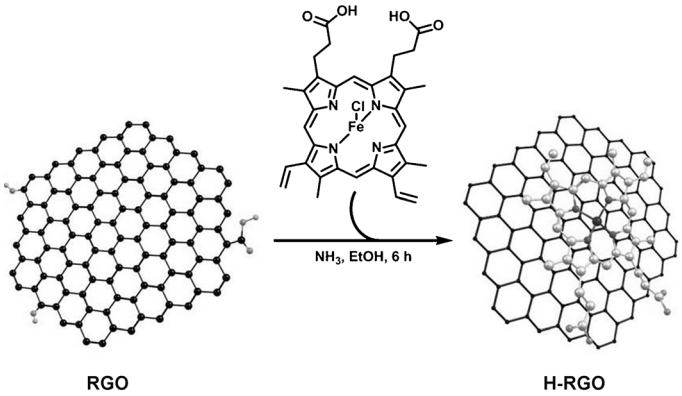

Scheme 3. Schematic representation of the synthesis of H-RGO nanosheets.

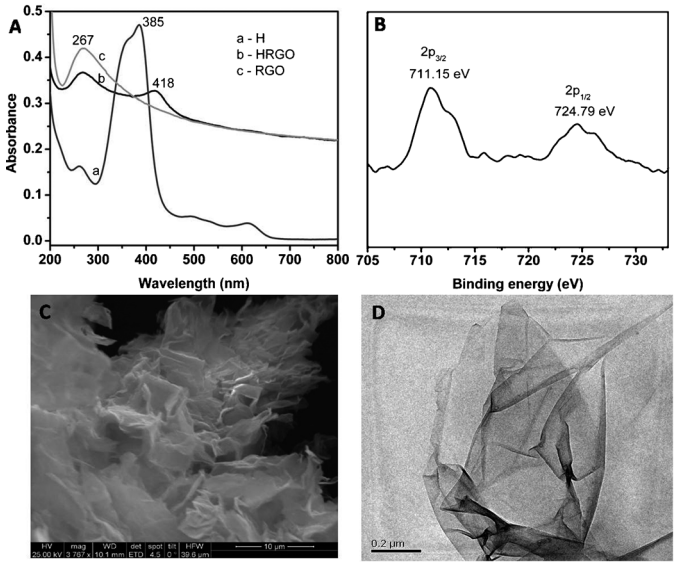

Figure 9. A) UV/Vis spectra of a) hemin, b) H-RGO, and c) RGO. B) Peaks of Fe2P in XPS of H-RGO. C), D) SEM and TEM images of H-RGO, respectively.

The non-covalently grafted hemin on RGO was characterized by various methods. The UV/Vis spectrum (Figure 9A) reveals a bathochromic shift of soret band of hemin from 385 nm to 418 nm with very weak Q bands. The large bathochromic shift of 33 nm is observed due to π--π stacking interaction between graphene and hemin as reported in the literature.[5a] The estimated amount of hemin on RGO was found to be 1.42% as calculated by comparing the absorbance of hemin and H-RGO after the blank correction with RGO. Owing to the noncovalent interactions between RGO and hemin in H-RGO, the D and G bands are shifted slightly to 1352 cm^{-1} and 1590 cm^{-1}, respectively as observed from Raman spectra of H-RGO (Figure S4 in the Supporting Information). There is no apparent change in the I_D/I_G ratio of H-RGO (1.04) and RGO (1.06), thus indicating the conservation of conjugation upon functionalization of RGO with hemin as reported elsewhere for Picket–Fence porphyrin functionalized graphene hybrid.[25] Upon cyclic voltammetry, H-RGO nanosheets exhibit redox peaks across the equivalent cathodic and anodic current intensities with formal potential [$E^{o\prime}$] equal to −0.44 V (vs. Ag/AgCl in saturated KCl) and peak to peak separation of 76 mV. On the other hand, bare glassy carbon electrode, RGO in N_2 saturated phosphate buffer (pH 7.4) did not show any such peaks (Figure S5 in the Supporting Information). X-ray photoelectron spectrum (XPS) of H-RGO shows peaks at 711.5 eV and 398.6 eV (Figure 9B), which can be attributed to Fe2p and N1s of hemin on H-RGO nanosheets with 1.35% loading of hemin on RGO (Figure S6 in the Supporting Information). The binding energy of Fe2p in hemin shows a shift from the reported values for hemin by approx. 1 eV, thus suggesting the existence of strong electronic interactions between hemin and RGO.[26] AFM image reveals the thickness of H-RGO nanosheets to be 1.2 nm (Figure S7 in the Supporting Information), which indicates the partial surface adsorption of hemin on both the accessible sides of the RGO layer. The SEM (Figure 9C) and TEM images (Figure 9D) of H-RGO hybrid showed flaky features with folded morphologies.

Having synthesized the H-RGO hybrid nanosheets, it was thought worthwhile to investigate the PN ($ONOO^-$) scavenging activity of this material. PN is a potent biological oxidizing and nitrating agent that is generated in vivo by a diffusion-controlled reaction of nitric oxide (•NO) and superoxide ($O_2^{\bullet-}$).[27] PN is known to induce DNA modification[28] and lipid peroxidation in biomembranes.[29] It can oxidize protein/non-protein thiols[30] and inactivate enzymes by nitration of tyrosine residues, which affect the signal transduction.[31,32] Although several small molecules such as ascorbate, methionine, cysteine, thioureas, selenium compounds, and metalloporphyrins have been shown to scavenge PN,[33] the effect of graphene-based nanomaterials on PN-mediated oxidation or nitration have not been investigated. Therefore, the inhibition of PN-mediated oxidation of dihydrorhodamine to rhodamine 123 was studied by fluorescence spectroscopy. The IC_{50} values (the amount of materials required to inhibit 50% of the oxidation) were obtained by plotting the % oxidation of DHR versus the amount of scavengers (Figure 10).

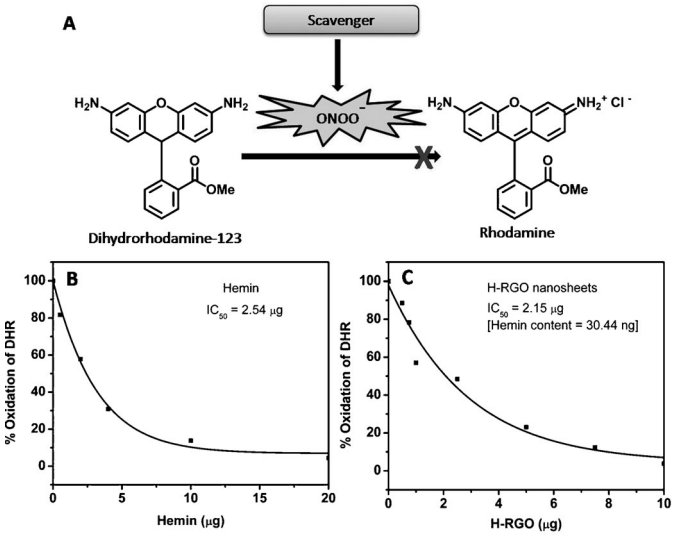

Figure 10. A) PN scavenging activity in PN-mediated oxidation of DHR to rhodamine 123 by scavengers. B),C) Activity plots of oxidation of DHR in the presence of H and H-RGO, respectively.

Interestingly, a remarkable PN scavenging activity with an IC_{50} value of 2.15 ± 0.19 μg was observed for the H-RGO hybrid nanosheets in which the hemin content was only about 30.44 ng. In contrast, the IC_{50} value obtained for hemin in its isolated form was 2.54 ± 0.40 μg, which indicates that the PN scavenging activity of hemin is increased by about 84-fold upon functionalization with RGO. These observations suggest that RGO acts synergistically with hemin

in exhibiting the PN scavenging activity. This is probably due to the π donor property of graphene to the Fe center of hemin through cationic π interactions.[5b] Such a synergistic effect has been demonstrated previously for a selective and quantitative cancer cell detection using folic acid conjugated graphene–hemin composite[5c] and oxidation of pyrogallol.[5b] In contrast to the H-RGO hybrid, RGO alone did not show any noticeable scavenging activity at lower concentrations. However, a significant decrease in the fluorescence intensity was observed at higher concentrations, thus indicating that RGO may quench fluorescence at higher concentrations.[34] In contrast to H-RGO nanosheets, GO and GO-hemin mixtures did not show any significant effect on the PN-mediated oxidation of DHR. These observations suggest that the π--π stacking interactions between the RGO and hemin play a significant role in the observed antioxidant effect.

In addition to the decomposition of PN in PN-mediated oxidation, we have also investigated the effect of H-RGO nanosheets on PN-mediated nitration by using free L-tyrosine by UV/Vis spectroscopy. The nitration of tyrosine has attracted immense interest in biology as nitrotyrosine has been extensively used as a potential biomarker for oxidative and nitrosative stress.[35] Furthermore, the formation of 3-nitrotyrosine has been implicated in different pathophysiological states such as neurological disorders, multiple sclerosis, atherosclerosis, Parkinson's disease, viral infections, rejection of transplanted organ, ischemia reperfusion injury.[36] Nitration of protein-bound tyrosyl residue is also known to inactivate enzymes such as mitochondrial ATPase, tyrosine hydroxylase, tyrosine kinase, α-thrombin, cytochrome P450, manganese superoxide dismutase.[32b,37] In the present study, when free hemin was tested as a scavenger of PN in PN-mediated nitration of free L-tyrosine, no scavenging activity was observed (Figure 11). In fact, an increase in the formation of 3-nitro-L-tyrosine upon supplement of 1 μg to 50 μg hemin was observed, indicating that free hemin catalyzes the formation of 3-nitro-L-tyrosine. Interestingly, when H-RGO was employed as a scavenger, the IC_{50} value of 2.50 ± 0.04 μg with hemin content of 35.40 ng was obtained. The PN scavenging properties of H-RGO nanosheets in the nitration reactions are similar to that observed for the oxidation reaction. As mentioned earlier, synergistic effect of H-RGO plays a major role in scavenging of PN in these potentially harmful PN-mediated reactions.

To understand whether the H-RGO nanosheets can scavenge PN in PN-mediated nitration of tyrosine residues in proteins, we investigated the inhibition of PN-mediated nitration of bovine serum albumin (BSA). As BSA contains several tyrosyl residues that could be targets for nitration, the PN-mediated nitration of this protein has been studied extensively. The H-RGO hybrid nanosheets exhibited 70% scavenging activity in the PN-mediated nitration reaction as seen from Figure 12. In contrast, hemin and RGO showed only 6.90 ± 0.21% and 21.49 ± 0.92% scavenging activity, respectively (Figure 12). As the oxidation of the Fe^{III} center in heme is expected to produce the corresponding Fe^{IV}-oxo species, a catalytic reduction of $ONOO^-$ to NO_2^- can be

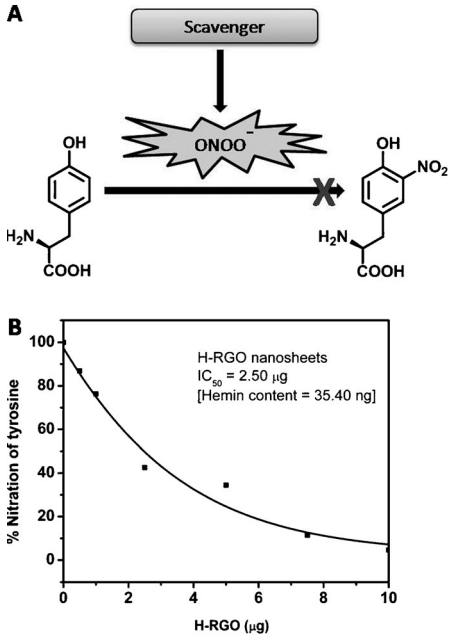

Figure 11. A) PN scavenging activity in PN-mediated nitration of free L-tyrosine to 3-nitro-L-tyrosine. B) Activity plots of nitration of free L-tyrosine in the presence of various concentrations of H-RGO.

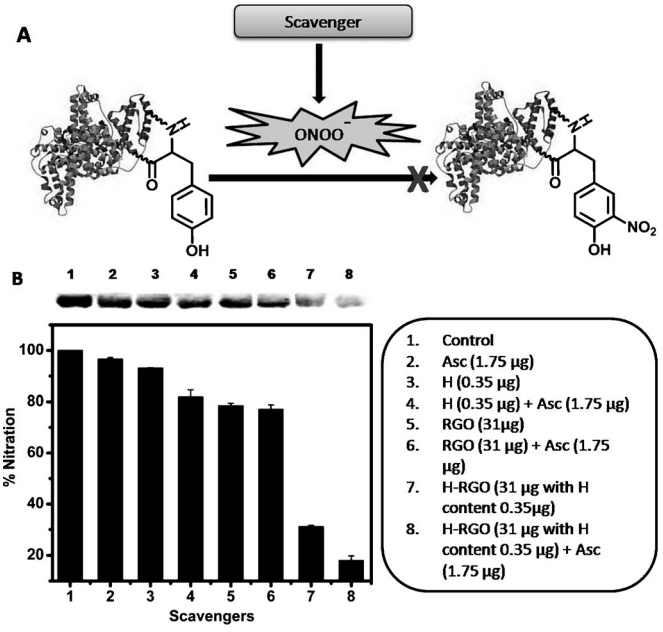

Figure 12. A) PN scavenging activity in PN-mediated nitration of tyrosyl residue in BSA by scavengers. B) Anti-nitrotyrosine immunoblotting of BSA after treatment with PN in the absence and presence of scavengers. H-RGO having 1.13% of hemin content was used.

achieved by reducing the Fe^{IV} center in the oxidized H-RGO to Fe^{III}. Therefore, we have studied the effect of ascorbic acid (Asc), a reducing agent, on PN-scavenging activity of H-RGO nanosheets. When an excess amount of Asc was added, the scavenging activity of hemin and H-RGO nanosheets was enhanced by approximately 10 and 12%, re-

spectively. However, there was no significant enhancement in the activity when only Asc was added to RGO. These observations indicate that PN reacts with the Fe^{III} center in H-RGO to produce the corresponding Fe^{IV}-oxo species and the conversion of PN to NO_2^- becomes catalytic in the presence of Asc. The efficient isomerization and catalytic reduction of PN by H-RGO can be ascribed to the π–π stacking interactions between RGO and hemin. The ability of RGO to attract nitrogen oxides may also contribute to the enhanced activity of H-RGO nanosheets.[38] In the absence of RGO, hemin has a tendency to form stable oxo or peroxo dimers on reaction with peroxynitrite or other oxidizing agents.[39] In the case of H-RGO hybrid nanosheets, the π–π stacking may disfavor the formation of stable oxo and peroxo dimmers. Furthermore, the H-RGO hybrid can be considered as a catalyst for the isomerization of PN to NO_3^- as these nanosheets having only 350 ng of hemin content prevents nitration by almost 70% nitration even in the presence of very high (1800 μM) concentration of PN.

It is known that hemin can enhance the nitration of tyrosine residues in proteins by NO_2^- and H_2O_2.[40] In agreement with this, a significant increase in the tyrosine nitration was observed when free hemin was added to BSA, $NaNO_2$, and H_2O_2 (Figure S8 in the Supporting Information). In contrast, a marginal decrease in the nitration with respect to the control was observed in the presence of RGO. Interestingly, a further decrease in the nitration was observed when H-RGO was used instead of RGO. These observations indicate that the π–π stacking interactions between RGO and hemin significantly alter the redox properties of hemin. It should be noted that heme peroxidases such as myeloperoxidase (MPO) and horseradish peroxidase (HRP) utilize NO_2^- and H_2O_2 as substrates to catalyze tyrosine nitration in proteins.[41] Recently, Guo et al. have shown that hemin-graphene nanosheets can catalyze the oxidation of different peroxidase substrates such as 2,2′-azinobis(3-ethylbenzothiozoline)-6-sulfonic acid (ABTS), and 3,3′,5,5′-tetramethylbenzidine (TMB) and *o*-phenylenediamine (OPD) in the presence of H_2O_2.[5a] However, in the presence of NO_2^- and H_2O_2, the heme in H-RGO hybrid appears to behave differently from that of heme peroxidases.

The mechanism for the reduction/isomerization of PN by H-RGO nanosheets appears to be similar to the one proposed for an iron–porphyrin complex.[4b] According to this mechanism (Scheme 4), the Fe^{III} center in the H-RGO reacts with PN to generate Fe^{III}-O-ONO species. The homolysis of the O–O bond in this species leads to the formation of caged radical $Fe^{IV}=O^{\bullet}NO_2$ intermediate. As mentioned earlier, the RGO layers may help in increasing the local concentration of nitrite and decreasing their escape, which may facilitate the recombination of $Fe^{IV}=O$ and nitrite. It has been shown previously that graphene-based nanocomposites can be used as selective sensors for nitrite anions.[42] Therefore, the recombination of Fe^{IV}=O and $^{\bullet}NO_2$ generates the Fe^{III}-nitrato complex. The cleavage of the Fe–O bond in the Fe^{III}–ONO_2 species regenerates the Fe^{III} center with an elimination of nitrate (NO_3^-). In the presence of ascorbic acid, the reduction of Fe^{IV}=O intermediate can also regenerate the Fe^{III} with the elimination of NO_2^- as shown in Scheme 4. The major effect of graphene is the minimization of the $^{\bullet}NO_2$ cage escape reaction that is generally observed for free heme and heme proteins. It should be noted that the rapid diffusion of $^{\bullet}NO_2$ from the heme site is responsible for the tyrosine nitration.

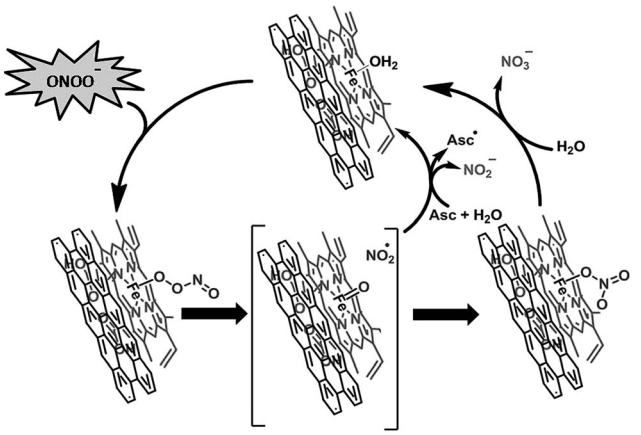

Scheme 4. Proposed mechanism for the isomerization and reduction of PN and scavenging of $\cdot NO_2$ by H-RGO hybrid nanosheets. Asc = ascorbic acid.

The changes between the two redox states of heme can be studied by UV/Vis spectroscopy. When PN (1000 μM) was added to H-RGO (30 μg) in assay buffer (pH 7.4), immediate decrease in the intensity of soret band of hemin in H-RGO was observed, suggesting the formation of $Fe^{IV}=O$ species with relative depletion of Fe^{III} species (Figure S9 in the Supporting Information). After about 50 s of reaction time, a further increase in the absorbance due to soret band was noted, which indicates that the $Fe^{IV}=O$ species is reduced back to Fe^{III}. A possible reason for the change in the oxidation state is the recombination of $^{\bullet}NO_2$ with the $Fe^{IV}=O$ species, which generates nitrate (isomerization mechanism). The oxidation of the Fe^{III} species with H_2O_2 (1000 μM) shows a decrease in absorbance of soret band due to the formation of the $Fe^{IV}=O$ species (Figure S10 in the Supporting Information). When excess $NaNO_2$ (2000 μM) was added to the reaction mixture containing H-RGO (30 μg) and H_2O_2 (1000 μM), an increase in absorbance was noted after few seconds (Figure S11 in the Supporting Information). This increase is probably due to the reduction of $Fe^{IV}=O$ to Fe^{III} with the generation of nitrate.

Conclusion

In this article, a facile and efficient approach for the synthesis of RGO by the reduction of GO using DTT has been described. The strong reducing ability of DTT is attributed to the generation of reactive dithiolates in reaction and thermodynamic stability of disulfide state after the reduction of GO. The reduction by DTT is very efficient than that ach-

ieved using glutathione and cysteine. Spectroscopic studies of RGO confirm the effective removal of oxygen containing functionalities in GO. Microscopic examination reveals the formation of few (2–4) layers of RGO (due to corrugation and scrolling) with pronounced crystallinity. The reduction of GO by DTT appears to be a good method for the preparation of good quality RGO in good yield. Noncovalent functionalization of RGO with hemin resulted in material that exhibits a remarkable antioxidant activity under physiologically relevant conditions. The stabilization of monomeric hemin on RGO provides the required synergistic effect for an efficient isomerization and reduction of PN. The $^{\bullet}NO_2$ scavenging action of H-RGO nanosheets together with the recombination of NO_2 and $Fe^{IV}=O$ to form nitrate contribute to the observed antioxidant effect.

Experimental Section

Chemicals: Graphite (2–15 μm) and DTT were purchased from Alfa Aesar and used as received. Sulfuric acid, hydrochloric acid, and potassium permanganate were purchased from S. D. Fine chemicals. Hydrogen peroxide used in the study was purchased from Merck. Tyrosine used in the nitration experiments was obtained from Calbiochem. BSA, sodium nitrite and isoamyl nitrite were purchased from Sigma–Aldrich.

Characterization methods: Absorption spectra were recorded on a Perkin–Elmer Lambda 750 UV/Vis spectrometer. IR spectra were obtained on a Bruker IR spectrometer. Raman spectroscopy was performed on a HORIBA JOBIN YVON LabRAM HR Raman spectrometer. Powder XRD was recorded on PANalytical Xpert pro theta-two theta diffractometer using a $Cu_{K\alpha}$ (1.5406 Å) radiation. CV was performed on EG and G PAR Model 253 Versa stat/potentiostat/galvanostat with electrochemical analysis software 270. A three-electrode system was used in the experiment with a bare and the modified glassy carbon electrode (3 mm diameter) as the working electrode, respectively. An Ag/AgCl electrode (saturated KCl) and a Pt wire electrode were used as a reference and counter electrode, respectively. X-ray photoelectron spectroscopy (XPS) was carried out on a MULTLAB 2000 THERMO SCIENTIFIC, UK. Thermogravimetric analysis (TGA) was carried out on a NETZSCH TG 209 F1 instrument at a heating rate of 2 °C min^{-1} from 40–750 °C. Solid state ^{13}C magic-angle spinning (MAS) NMR spectra were obtained from 300 MHz Bruker Avance solid state NMR spectrometer using standard Bruker pulse programs. Atomic-force microscopy (AFM) measurements were performed using Nanoscope V multimode atomic force microscope (Veeco Instruments, USA) operating in the tapping mode. Scanning electron microscopy (SEM) images were recorded on Fei Sirion UHR SEM. Transmission electron microscopy (TEM) images and SAED pattern were recorded on Fei Tecnai T20 Ultra Twin operating at 200 kV after casting a drop of RGO dispersion in ethanol over Cu grid.

Preparation of GO: The graphite oxide was synthesized from graphite powder following the Hummers method.[6] Typically, concentrated H_2SO_4 (69 mL) was added to a mixture of graphite powder (3.0 g) and $NaNO_3$ (1.5 g) and the mixture was cooled to 0 °C. $KMnO_4$ (9.0 g) was added slowly in portions to keep the reaction temperature below 20 °C. The reaction was warmed to 35 °C and stirred for 30 min, at which time water (138 mL) was added slowly, producing a large exotherm to 98 °C. External heating was introduced to maintain the reaction temperature at 98 °C for 15 min, then the heating was removed and the reaction was cooled using water bath for 10 min. Additional water (420 mL) and 30% H_2O_2 (3 mL) were added, producing another exotherm and to produce bright yellow precipitate. This mixture was cooled to room temperature and centrifuged at 4000 rpm. The yielded brownish-yellow precipitate of GO was washed several times with 5% HCl and then with water/ethanol and finally dried in air. GO obtained was subjected to ultrasonication for 40 min (20% amplitude) in order to exfoliate into graphene oxide in ultrapure water. Homogeneous dispersion of GO (1 mg mL^{-1}) obtained was directly used for reduction to get RGO nanosheets.

Preparation of RGO: Reduction of GO was achieved by using DTT. Typically, 200 mg DTT was added to 100 mL of homogeneous GO dispersion (1 mg mL^{-1}). The pH of this dispersion was maintained above 9 by the addition of 30% ammonia solution and stirred vigorously for 10 min at 30 °C. Then, the temperature was raised to 80 °C and maintained for 1 h. The brown dispersion of GO changed to black in color upon reduction with DTT. The RGO was centrifuged (8000 rpm) and washed several times with ultrapure water and finally with ethanol and then dried in air.

Synthesis of H-RGO hybrid nanosheets: Hemin (2 mg) was firstly dissolved in 10 mL ethanol by the addition of 80 μL NH_3 to get dark reddish-brown solution. To this, 40 mg of RGO was added and the reaction mixture was sonicated for 5 min to ensure the complete dispersion of RGO. Stirring was continued at room temperature for 6 h. Centrifugation at 12000 rpm for 15 min resulted in separation of precipitate, which was washed five times with ammoniated ethanol to remove excess hemin and finally with ethanol to yield H-RGO nanosheets.

Preparation of RGO and H-RGO modified electrode: The RGO and H-RGO modified electrode was prepared by a method described elsewhere.[5a] The glassy carbon electrode (3 mm) was polished with alumina slurry, rinsed with ultrapure water. Further, it was washed successively with 1:1 nitric acid, acetone, and ultrapure water in an ultrasonic bath and dried in air. The RGO and H-RGO modified glassy carbon electrodes were obtained by casting a drop of 5 mg mL^{-1} suspension (methanol) on the surface of electrode, which were dried in air. Finally, the modified electrodes were activated by several successive scans with a scan rate of 50 mV s^{-1} in phosphate buffer solution (pH 7.4) until a steady voltammogram was obtained.

Synthesis of peroxynitrite (PN): Peroxynitrite was synthesized by following the literature method with minor modifications.[43] A solution of 30% (ca. 8.8 M) H_2O_2 was diluted to 50 mL with water, cooled to about 4 °C in an ice/water mixture, added to NaOH (5N, 30 mL), and diethylene triamine pentaacetic acid (DTPA; 0.04 M, 5 mL) in NaOH (0.05 N) with gentle mixing, and then diluted to a total volume of 100 mL. The concentration of H_2O_2 in the final solution was 0.5 M; the pH ranged from 12.5 to 13.0. The buffered H_2O_2 was stirred vigorously with an equimolar amount of isoamyl nitrite (0.05 M or 6.7 mL) for 3–4 h at room temperature. The reaction was monitored by withdrawing aliquots at an interval of 15 or 30 min and assaying for peroxynitrite at 302 nm using UV/Vis spectrophotometer. When the yield of peroxynitrite reached a maximum, the aqueous phase was washed with dichloromethane, chloroform, and hexane (3 × 100 mL) in a separating funnel to remove the contaminating isoamyl alcohol and isoamyl nitrite. The unreacted H_2O_2 was removed by passing the aqueous phase through a column filled with granular MnO_2 (25 g). The concentration of the stock solution of peroxynitrite was measured after 500 times dilution with a NaOH solution (0.1 N) and then assaying for peroxynitrite at 302 nm ($\varepsilon = 1670\ M^{-1}cm^{-1}$) using the UV/Vis spectrophotometric method.

PN scavenging activity in PN mediated oxidation of dihydrorhodamine: PN-mediated oxidation of dihydrorhodamine (DHR) was studied using fluorescence spectroscopy. Fluorescence intensity was measured with excitation and emission wavelengths of 500 nm and 526 nm, respectively. The stock solution of DHR in dimethylformamide was purged with nitrogen and stored at −20 °C. The working solutions of DHR and PN were kept on ice bath. The assay mixture contained DHR (0.50 μM), PN (0.95 μM) in 100 mM phosphate buffer of pH 7.4 and variable inhibitor concentrations. The fluorescence intensity from the reaction of DHR with PN was set as 100% and the intensity after the addition of various scavengers was expressed as the percentage of the intensity observed in the absence of scavengers. The final fluorescence intensities were corrected for background reactions. The activity plots were obtained using Origin 6.1 software utilizing sigmoidal curve fitting and these plots were used for the determination of IC_{50} values.

PN scavenging activity in PN-mediated nitration of free L-tyrosine: PN-mediated nitration of free L-tyrosine was studied using UV/Vis spectro-

scopy. We employed a mixture containing L-tyrosine (1 mM) and PN (1.5 mM) in sodium phosphate buffer (100 mM) of pH 7.5 without and with increasing concentration of scavenger at 22 °C. It was incubated for 5 min before recording absorbance. The formation of 3-nitro-L-tyrosine was monitored at the wavelength 440 nm. The activity plots were obtained using origin 6.1 software utilizing sigmoidal curve fitting and then plots were used for the determination of IC_{50} values.

PN scavenging activity in PN-mediated protein (BSA) nitration: For bovine serum albumin (BSA), the nitration was performed by the addition of PN (1.8 mM) to BSA (133.3 μM) in 0.5 M phosphate buffer of pH 6.9 at 20 °C. After the addition of PN, the final pH was maintained below 7.5. The reaction mixture was incubated for 20 min at 22 °C. Similarly, the reactions of BSA with PN were performed in the presence of different scavengers. After the reactions, the mixture was denatured by boiling at 100 °C for 5 min in the presence of sample loading dye and subjected to polyacrylamide gel electrophoresis and immunoblot analyses.

Activity of scavengers in H_2O_2/nitrite mediated nitration of BSA: For bovine serum albumin (BSA), the nitration was performed by the addition of H_2O_2 (1.5 mM) and $NaNO_2$ (1.5 mM) to BSA (133.3 μM) in 0.5 M phosphate buffer of pH 6.9 at 20 °C. After the addition of PN, the final pH was maintained below 7.5. The reaction mixture was incubated for 20 min at 22 °C. Similarly, the reactions of BSA with H_2O_2/$NaNO_2$ were performed in the presence of different scavengers. After the reactions, the mixture was denatured by boiling at 100 °C for 5 min in the presence of sample loading dye and subjected to polyacrylamide gel electrophoresis and immunoblot analyses.

Gel electrophoresis and immunoblotting: Gel was prepared with 10% polyacrylamide with 6% stacking gel for BSA. The gel was run in the running buffer of pH 8.3 with glycine and SDS. After separating the proteins, the gel was analyzed by Immunoblotting experiments. The proteins were transferred to a PVDF membrane and the non-specific binding sites were blocked by 5% non-fat skimmed milk in PBST (blocking solution) for 1 h. Then the membrane was probed with rabbit polyclonal primary antibody against 3-nitro-tyrosine (1:20000 dilutions) in blocking solution for 2 h followed by incubation with horseradish peroxidase-conjugated donkey polyclonal anti-rabbit IgG (1:20000 dilutions) for another 1 h. The probed membrane was washed three times with blocking solution with 0.1% Tween 20 after each of the above steps and the immunoreactive protein was then detected by luminol-enhanced chemiluminescence (ECL, Amersham).

Acknowledgements

This study was supported by the Department of Science and Technology (DST) of New Delhi and AstraZeneca. G.M. acknowledges the DST for the award of a Swarnajayanti Fellowship, and A.A.V. thanks the Council of Scientific and Industrial Research (CSIR) of New Delhi for a research fellowship. We also acknowledge Prof. A. R. Chakravarty and Prof. N. Munichandraiah for providing cyclic voltammetry facility and Dr. S. N. Dhuri for providing a rapid scan UV/Vis spectrophotometry facility.

[1] a) X. Li, X. Wang, L. Zhang, S. Lee, H. Dai, *Science* **2008**, *319*, 1229–1232; b) S. Stankovich, D. Dikin, G. Dommett, K. Kohlhaas, E. Zimney, E. Stach, R. Piner, S. Nguyen, R. Ruoff, *Nature* **2006**, *442*, 282–286; c) F. Wang, Y. Zhang, H. Tian, C. Girit, A. Zettl, M. Crommie, Y. Shen, *Science* **2008**, *320*, 206–209; d) S. Guo, S. Dong, *Chem. Soc. Rev.* **2011**, *40*, 2644–2672; e) S. Guo, S. Dong, E. Wang, *ACS Nano* **2010**, *4*, 547–555; f) Y. Song, K. Qu, C. Zhao, J. Ren, X. Qu, *Adv. Mater.* **2010**, *22*, 2206–2210; g) Z. Liu, J. Robinson, X. Sun, H. Dai, *J. Am. Chem. Soc.* **2008**, *130*, 10876–10877; h) K. Loh, Q. Bao, P. Ang, J. Yang, *J. Mater. Chem.* **2010**, *20*, 2277–2289; i) Z. Tang, H. Wu, J. Cort, G. Buchko, Y. Zhang, Y. Shao, I. Aksay, J. Liu, Y. Lin, *Small* **2010**, *6*, 1205–1209; j) Q. Su, S. Pang, V. Alijani, C. Li, C. Feng, K. Mullen, *Adv. Mater.* **2009**, *21*, 3191–3195.

[2] a) K. S. Kim, Y. Zhao, H. Jang, S. Y. Lee, J. M. Kim, K. S. Kim, J.-H. Ahn, P. Kim, J.-Y. Choi, B. H. Hong, *Nature* **2009**, *457*, 706–710; b) P. W. Sutter, J.-I. Flege, E. A. Sutter, *Nat. Mater.* **2008**, *7*, 406–411; c) K. S. Novoselov, A. K. Geim, S. V. Morozov, D. Jiang, Y. Zhang, S. V. Dubonos, I. V. Grigorieva, A. A. Firsov, *Science* **2004**, *306*, 666–669; d) C. Berger, Z. Song, X. Li, X. Wu, N. Brown, C. Naud, D. Mayou, T. Li, J. Hass, A. N. Marchenkov, *Science* **2006**, *312*, 1191–1196; e) M. Lotya, Y. Hernandez, P. J. King, R. J. Smith, V. Nicolosi, L. S. Karlsson, F. M. Blighe, S. De, Z. Wang, I. T. McGovern, G. S. Duesberg, J. N. Coleman, *J. Am. Chem. Soc.* **2009**, *131*, 3611–3620.

[3] a) S. Park, R. S. Ruoff, *Nat. Nanotechnol.* **2009**, *4*, 217–224; b) Y. Si, E. T. Samulski, *Nano. Lett.* **2008**, *8*, 1679–1682; c) H. J. Shin, K. K. Kim, A. Benayad, S. M. Yoon, H. K. Park, I. S. Jung, M. H. Jin, H. K. Jeong, J. M. Kim, J. Y. Choi, *Adv. Func. Mater.* **2009**, *19*, 1987–1992; d) S. Stankovich, D. A. Dikin, R. D. Piner, K. A. Kohlhass, A. Kleinhammes, Y. Jia, Y. Wu, S. T. Nguyen, R. S. Ruoff, *Carbon* **2007**, *45*, 1558–1565; e) V. C. Tung, M. J. Allen, Y. Yang, R. B. Knaer, *Nat. Nanotechnol.* **2009**, *4*, 25–29; f) G. X. Wang, J. Yang, J. Park, X. L. Gou, W. Bang, H. Liu, J. Yao, *J. Phys. Chem. C* **2008**, *112*, 8192–8195; g) Z. Fan, W. Kai, J. Yan, T. Wei, L.-J. Zhi, J. Feng, Y.-M. Ren, L.-P. Song, F. Wei, *ACS Nano* **2011**, *5*, 191–198.

[4] a) G. Zhang, K. Dasgupta, *Anal. Chem.* **1992**, *64*, 517–522; b) M. Stern, M. Jensen, K. Kramer, *J. Am. Chem. Soc.* **1996**, *118*, 8735–8736.

[5] a) Y. Guo, L. Deng, J. Li, S. Guo, E. Wang, S. Dong, *ACS Nano* **2011**, *5*, 1282–1290; b) T. Xue, S. Jiang, Y. Qu, Q. Su, R. Cheng, S. Dubin, C.-Y. Chiu, R. Kaner, Y. Huang, X. Duan, *Angew. Chem. Int. Ed.* **2012**, *51*, 3822–3825; c) Y. Song, Y. Chen, L. Feng, J. Ren, X. Qu, *Chem. Commun.* **2011**, *47*, 4436–4438.

[6] W. Hummers, R. Offeman, *J. Am. Chem. Soc.* **1958**, *80*, 1339–1339.

[7] X. B. Fan, W. C. Peng, Y. Li, X. Y. Li, S. L. Wang, G. L. Zhang, F. B. Zhang, *Adv. Mater.* **2008**, *20*, 4490–4493.

[8] D. R. Dreyer, H.-P. Jia, A. D. Todd, J. Geng, W. Bielawski, *Org. Biomol. Chem.* **2011**, *9*, 7292–7295.

[9] a) F. Tuinstra, J. L. Koenig, *J. Chem. Phys.* **1970**, *53*, 1126–1130; b) K. N. Kudin, B. Ozbas, H. C. Schniepp, R. K. Prud'homme, I. A. Aksay, R. Car, *Nano Lett.* **2008**, *8*, 36–41; c) Z. Lin, Y. Yao, Z. Li, Y. Liu, Z. Li, C. P. W, *J. Phys. Chem. C* **2010**, *114*, 14819–14825.

[10] a) J. Zhang, H. Yang, G. Shen, P. Cheng, J. Zhang, S. Guo, *Chem. Commun.* **2010**, *46*, 1112–1114.

[11] J. Yan, Z. J. Fan, T. Wei, W. Z. Qian, M. Zhang, F. Wei, *Carbon* **2010**, *48*, 3825–3833.

[12] W. Gao, L. B. Alemany, L. Ci, P. M. Ajayan, *Nat. Chem.* **2009**, *1*, 403–408.

[13] M. Choucair, P. Thordarson, J. A. Stride, *Nat. Nanotechnol.* **2009**, *4*, 30–33.

[14] Y. Zhou, Q. L. Bao, L. A. L. Tang, Y. L. Zhong, K. P. Loh, *Chem. Mater.* **2009**, *21*, 2950–2956.

[15] D. Chen, L. Li, L. Guo, *Nanotechnology* **2011**, *22*, 325601.

[16] Y. K. Kim, M. H. Kim, D. H. Min, *Chem. Commun.* **2011**, *47*, 3195–3197.

[17] P. Khanra, T. Kuila, N. H. Kim, S. H. Bae, D.-S. Yu, J. H. Lee, *Chem. Eng. J.* **2012**, *183*, 526–533.

[18] T. A. Pham, J. S. Kim, J. S. Kim, Y. T. Jeong, *Colloids Surf. A* **2011**, *384*, 543–548.

[19] T. A. Pham, B. C. Choi, K. T. Lim, Y. T. Jeong, *Appl. Surf. Sci.* **2011**, *257*, 3350–3357.

[20] Z. Lei, L. Lu, X. S. Zhao, *Energy Environ. Sci.* **2012**, *5*, 6391–6399.

[21] a) G. Wang, X. Shen, B. Wang, J. Yao, J. Park, *Carbon* **2009**, *47*, 1359–1364; b) J. C. Meyer, A. K. Geim, M. I. Katsnelson, K. S. Novoselov, T. J. Booth, S. Roth, *Nature* **2007**, *446*, 60–63.

[22] Y. Hernandez, V. Nicolosi, M. Lotya, F. M. Blighe, Z. Sun, S. De, *Nat. Nanotechnol.* **2008**, *3*, 563–568.

[23] a) J. I. Paredes, S. Villar-Rodil, P. Solís-Fernández, A. Martínez-Alonso, J. M. D. Tascón, *Langmuir* **2009**, *25*, 5957–5968; b) H. He, T. Riedl, A. Lerf, J. Klinowski, *J. Phys. Chem.* **1996**, *100*, 19954–19958; c) H. He, J. Klinowski, M. Forster, A. Lerf, *Chem. Phys. Lett.* **1998**, *287*, 53–56; d) A. Lerf, H. He, T. Riedl, M. Forster, J. Kinowk-

si, *Solid State Ionics* **1997**, *101–103*, 857–862; e) A. Lerf, H. He, M. Forster, J. Kinowksi, *J. Phys. Chem. B* **1998**, *102*, 4477–4482.
[24] D. Li, M. B. Müller, S. Gilje, R. B. Kaner, G. G. Wallace, *Nat. Nanotechnol.* **2008**, *3*, 101–105.
[25] W. Tu, J. Lei, S. Zhang, H. Ju, *Chem. Eur. J.* **2010**, *16*, 10771–10777.
[26] Z. Liang, H. Song, S. Liao, *J. Phys. Chem. C* **2011**, *115*, 2604–2610.
[27] a) R. Huie, S. Padmaja, *Free Radical Res. Commun.* **1993**, *18*, 195–199; b) R. Kissner, T. Nauser, P. Bugnon, P. Lye, W. Koppenol, *Chem. Res. Toxicol.* **1997**, *10*, 1285–1292.
[28] a) T. Douki, J. Caket, B. Ames, *Chem. Res. Toxicol.* **1996**, *9*, 3–7; b) B. Epe, D. Ballmaier, I. Rous *syn*, K. Briviba, H. Sies, *Nucleic Acids Res.* **1996**, 24, 4105–4110.
[29] a) R. Radi, J. Beckman, K. Bush, B. Freeman, *Arch. Biochem. Biophys.* **1991**, *288*, 481–486; b) P. K. Moore, V. Darley-Usmar, J. Morrow, L. J. Roberts II, *Circ. Res.* **1995**, ***77***, 335–341.
[30] a) R. Radi, J. S. Beckman, K. M. Bush, B. A. Freeman, *J. Biol. Chem.* **1991**, *266*, 4244–4250; b) C. Quijano, B. Alvarez, R. M. Gatti, O. Augusto, R. Radi, *Biochem. J.* **1997**, *322*, 167–173; c) D. M. Kuhn, C. W. Aretha, T. J. Geddes, *J. Neurosci.* **1999**, *19*, 10289–10294.
[31] a) L. MacMillan-Crow, J. Crow, J. Kerby, J. Beckman, J. Thompson, *Proc. Natl. Acad. Sci. USA* **1996**, *93*, 11853–11858; b) L. MacMillan-Crow, J. Crow, J. Thompson, *Biochemistry* **1998**, *37*, 1613–1622.
[32] a) S. Kong, M. Yim, E. Stadtman, P. Chock, *Proc. Natl. Acad. Sci. USA* **1996**, *93*, 3377–3382; b) A. Gow, D. Duran, S. Malcolm, H. Ischiropoulos, *FEBS Lett.* **1996**, *385*, 63–66.
[33] a) W. Pryor, X. Jin, G. L. Squadritio, *Proc. Natl. Acad. Sci. USA* **1994**, *91*, 11173–11177; b) V. Lymar, J. K. Hurst, *J. Am. Chem. Soc.* **1995**, *117*, 8867–8868; c) K. Briviba, L.-O. Klotz, H. Sies, *Methods Enzymol.* **1999**, *301*, 301–310; d) K. Bhabak, G. Mugesh, *Chem. Eur. J.* **2010**, *16*, 1175–1185; e) B. Sarma, D. Manna, M. Minoura, G. Mugesh, *J. Am. Chem. Soc.* **2010**, *132*, 5364–5374; f) K. Satheeshkumar, G. Mugesh, *Chem. Eur. J.* **2011**, *17*, 4849–4857; g) K. P. Bhabak, A. A. Vernekar, S. R. Jakka, G. Roy, G. Mugesh, *Org. Biomol. Chem.* **2011**, *9*, 5193–5200.
[34] H. S. S. Ramakrishna Matte, K. Subrahmanyam, S. George, C. N. R. Rao, *Chem. Phys. Lett.* **2011**, *506*, 260–264.
[35] a) A. van der Vliet, J. P. Eiserich, B. Halliwell, C. E. Cross, *J. Biol. Chem.* **1997**, *272*, 7617–7625; b) T. Brück, R. Fielding, M. Symons, P. Harvey, *Eur. J. Biochem.* **2001**, *268*, 3214–3222.
[36] T. Sawa, T. Akaike, H. Maeda, *J. Biol. Chem.* **2000**, *275*, 32467–32474 and references therein.
[37] a) G. Jänig, R. Kraft, J. Blanck, O. Ristau, H. Rabe, K. Ruckpaul, *Biochim. Biophys. Acta* **1987**, *916*, 512–523; b) R. Lundblad, C. Noyes, G. Featherstone, J. Harrison, J. Jenzano, *J. Biol. Chem.* **1988**, *263*, 3729–3734; c) F. Guerrieri, A. Yagi, T. Yagi, S. Papa, *J. Bioenerg. Biomembr.* **1984**, *16*, 251–262; d) J. Ara, S. Przedborski, A. Naini, V. J. ackson-Lewis, R. Trifiletti, J. Horwitz, H. Ischiropoulos, *Proc. Natl. Acad. Sci. USA* **1998**, *95*, 7659–7663; e) H. Ischiropoulos, L. Zhu, J. Chen, M. Tsai, J. Martin, C. Smith, J. Beckman, *Arch. Biochem. Biophys.* **1992**, *298*, 431–437.
[38] S. Ng, C. Guo, C. Li, *Electroanalysis* **2011**, *23*, 442–448.
[39] M. Jensen, D. Riley, *Inorg. Chem.* **2002**, *41*, 4788–4797.
[40] a) Y. Zhang, N. Lu, Z. Gao, *Int. J. Biochem. Cell Biol.* **2009**, *41*, 907–915; b) K. Bian, Z. Gao, N. Weisbrodt, F. Murad, *Proc. Natl. Acad. Sci. USA* **2003**, *100*, 5712–5712.
[41] J. B. Sampson, Y. Ye, H. Rosen, J. S. Beckman, *Arch. Biochem. Biophys.* **1998**, *356*, 207–213.
[42] D. Ye, L. Luo, Y. Ding, Q. Chen, X. Liu, *Analyst* **2011**, *136*, 4563–4569.
[43] a) R. M. Uppu, W. A. Pryor, *Anal. Biochem.* **1996**, *236*, 242–249; b) R. M. Uppu, *Anal. Biochem.* **2006**, *354*, 165–168.

Received: June 27, 2012
Published online: October 5, 2012

